Oxygen Vacancy-Enriched Amorphous Transition Metal Ternary Oxides toward Highly Efficient Oxygen Evolution Reaction

Qianyun Bai[†], Da Liu[†], Xiaoxiao Yan[†], Peifang Guo[†], Xingyu Ding[†], Kang Xiang[†], Xin Tu[‡], Yanhui Guo[†,*], and Renbing Wu[†,*]

[†]Department of Materials Science, Fudan University, 2005 Songhu Road, Shanghai 200438, P. R. China

[‡]Department of Electrical Engineering and Electronics, University of Liverpool, Liverpool L69 3GJ, UK

KEYWORDS: transition metal oxide; oxygen vacancy; amorphous; oxygen evolution reaction; electrolyzer

ABSTRACT: Developing highly efficient oxygen evolution reaction (OER) electrocatalysts based on earth-abundant elements is critical to improve the efficiency of water electrolysis but remains challenge. Herein, an amorphous ternary oxides composites $FeNiCoO_x/CoO_x$ with rich oxygen vacancies are developed through a low-cost wet chemical deposition strategy towards this challenge. Benefiting from synergistic effect of multi-metal atoms interaction and high exposure of active sites caused by oxygen vacancies and amorphous structure, the as-developed $FeNiCoO_x/CoO_x$ electrocatalyst exhibits an exceptional catalytic performance with a low overpotential of only 221 mV at a current density of 100 mA cm^{-2}, and negligible performance degradation over 240 hours. Furthermore, the $FeNiCoO_x/CoO_x$-assembled anion exchange membrane water electrolyzer (AEMWE) can achieve a high current density of 1 A cm^{-2} at a low voltage of 1.765 V, demonstrating its great potential for practical application.

Water electrolysis has been regarded as one of the most economical, sustainable and environmental-friendly energy conversion and storage technologies for relieving the conflict between energy demand and sustainable development.[1–4] Nevertheless, the anodic oxygen evolution reaction (OER) suffers from sluggish kinetics caused by multi-step proton-coupled electron transfer processes, which severely restrict the overall efficiency of water electrolysis.[5–7] Consequently, electrocatalysts that can accelerate kinetics and reduce energy barrier are key points to improve electrolysis efficiency.[8-9] Unfortunately, the state-of-the-art OER electrocatalysts based on noble metals (e.g. Ir and Ru) could not support large-scale application of water electrolysis on account of limited resource and high price.[10–13] Therefore, it is highly urgent to design low-cost OER electrocatalysts with high performance for the implementation of water splitting.

Transition metal oxides have been widely investigated as OER electrocatalysts due to their low costs and tunable electronic structures.[14–16] Considerable efforts have been made on optimizing component collocation, adjusting crystal and electron structure, and regulating morphology to further improve their catalytic performance.[17–19] In particular, introducing different metal elements to form muti-metallic oxides is considered as an effective approach to enhance intrinsic activities.[20–22] Compared with individual metal oxides, the electronic structures in multi-metallic oxide catalysts could be intensively modulated to optimize the adsorption energy of intermediates, thus demonstrating remarkable OER activities.[23–25] For instance, Duan et al. designed $ZnCo_{1.2}Ni_{0.8}O_4$ oxides and found that Ni substitution modified intrinsic property of the relative position between O p-band center and M_{Oh} d-band center, resulting in an enhanced OER activity.[26] Antink et al. synthesized a high-entropy oxide $(CrFeCoNiMo)_3O_4$ and verified that the incorporation of high-valence Cr and Mo could activate lattice oxygen by weakening metal-oxygen bond. The as-synthesized catalyst displayed a low overpotential of 255.3 mV at a current density of 10 mA cm^{-2} and excellent stability.[27]

The introduction of oxygen vacancies is regarded as another effective strategy to enhance OER electrocatalytic activities.[28,29] It has been well recognized that oxygen vacancies could promote exposure of active sites, improve conductivity and mass transfer, and thus are benefit to OER performances.[30,31] For example, Kang et al. prepared Co-based catalysts with abundant oxygen vacancies, which exhibited an improved OER performance owing to accelerated kinetics and charge transfer.[32] Li et al. synthesized a series of $Bi_{0.15}Sr_{0.85}Co_{1-x}Fe_xO_{3-\delta}$ perovskites and found that oxygen vacancies promoted the generation of reconstructed active layers, delivering a current density of 10 mA cm^{-2} at the overpotential of 290 mV.[33]

Recently, it has been demonstrated that short-range ordered structure and remarkable flexibility of amorphous surface could provide abundant unsaturated sites, accelerating both ion diffusion and electron transfer.[34-36] Additionally, amorphous structure possesses plentiful dangling bonds, leading to relatively higher surface energy compared to crystalline structure, which is favorable to the adsorption processes of catalytic reactions.[37–39] Liu et al. constructed a composite catalyst with amorphous surface of cobalt and

iron oxides and found that the adaptive amorphous surface structure was responsible for its good catalytic performance.[40] Li et al. reported an amorphous $Co(OH)_2/WO_x$ catalyst, affording a current density of 10 mA cm^{-2} at an overpotential of 208 mV. [41] Although prominent advantages have been made, the integration of multiple metal components, oxygen vacancies and amorphous structures to boost OER catalytic activity has rarely been achieved.

Herein, we creatively developed a convenient wet chemical deposition method to synthesize a composite catalyst constructed by amorphous ternary metal oxide $FeNiCoO_x$ with abundant oxygen vacancies on CoO_x supported by carbon paper (denoted as $FeNiCoO_x/CoO_x/CP$). Owing to accelerated electron transfer by synergistic interactions among Fe, Ni and Co components, optimized electronic structure and highly exposed active sites, the as-synthesized $FeNiCoO_x/CoO_x/CP$ exhibited a remarkable OER activity, with an ultra-low overpotential of 221 mV at a current density of 100 mA cm^{-2} and a small Tafel slope of 30 mV dec^{-1}. More importantly, the $FeNiCoO_x/CoO_x/CP$-assembled anion exchange membrane water electrolyzer (AEMWE) could drive a high current density of 1 A cm^{-2} at an impressively low voltage of only 1.765 V.

The amorphous $FeNiCoO_x/CoO_x/CP$ was synthesized through a two-step wet chemical deposition process, as illustrated in Figure S1. Initially, CoO_x was prepared onto the carbon paper (CP) substrate. As shown in the field-emission scanning electron microscopy (FESEM) images (Figure S2a and S2b), rough surface with uniformly dispersed particles of ~8 nm could be observed, which would be used as active nucleation sites in the subsequent chemical deposition of $FeNiCoO_x$. As depicted in Figure 1a and 1b, the ternary metal oxide $FeNiCoO_x$ exhibits a uniform three-dimensional (3D) porous network structure. Binary metal oxides $FeCoO_x$ and $NiCoO_x$ prepared through similar methods show similar 3D porous network (Figure S2c and S2d). The cross-section FESEM images (Figure 1c and Figure S3) clearly display the distinct morphological differences between CoO_x and $FeNiCoO_x$ layer. The optimized thicknesses of CoO_x (~2.8 μm) and $FeNiCoO_x$ layer (~2.5 μm) exhibit the best performance (Figure S4). Nitrogen physisorption methods were used to evaluate specific surface areas and pore sizes of the samples. As shown Figure S5a, the adsorption-desorption curve of $FeNiCoO_x/CoO_x/CP$ is a type-IV isotherm with a hysteresis loop at 0.4 of P/P_0, indicating its mesoporous structure.[42] The pore size distribution determined by the Barrett-Joyner-Halenda (BJH) model exhibits the mesopore feature of the as-synthesized $FeNiCoO_x/CoO_x$ ranging from 2 to 50 nm (Figure S5b), effectively promoting the mass transport.[43,44] The Brunauer-Emmett-Teller (BET) surface area of $FeNiCoO_x/CoO_x$ is 13.868 m^2 g^{-1}, much higher than that of CoO_x/CP (5.323 m^2 g^{-1}) (Figure S5c and S5d), suggesting more exposed active sites after the deposition of $FeNiCoO_x$. Surface charges of the materials measured by zeta potentials (Figure S6) indicate that they have a negligible effect on the catalytic performance. To evaluate the hydrophilicity of the surface of catalyst, the contact angles were also measured. As shown in Figure S7, the contact angle of $FeNiCoO_x/CoO_x/CP$ is 69.5°, much lower than those of CoOx/CP (133.9°) and pure CP (143.3°). The improved hydrophilicity may significantly promote charge transfer as well as the release of oxygen bubbles.

X-ray diffraction (XRD) was carried out to determine the phase structures of as-synthesized catalysts. As depicted in Figure 1d and Figure S8, no diffraction peak could be observed in all samples, indicating the possible formation of amorphous structure.[45] The amorphous $FeNiCoO_x/CoO_x$ and CoO_x structures were further investigated by high resolution transmission electron microscopy (HRTEM). As shown in Figure 1e and Figure S9a, the absence of lattice fringes along with ring-like characteristic observed in selected area electron diffraction (SAED) patterns (Figure 1f and Figure S9b) further verify the amorphous phases of both $FeNiCoO_x/CoO_x$ and CoO_x. High-angle annular dark-field scanning transmission electron microscopy (HAADF-STEM) and corresponding energy-dispersive spectroscopy (EDS) elemental mapping images and spectrum (Figure 1g and Figure S10) reveal the co-existence and uniform distribution of Fe, Co, Ni and O elements throughout the sample.

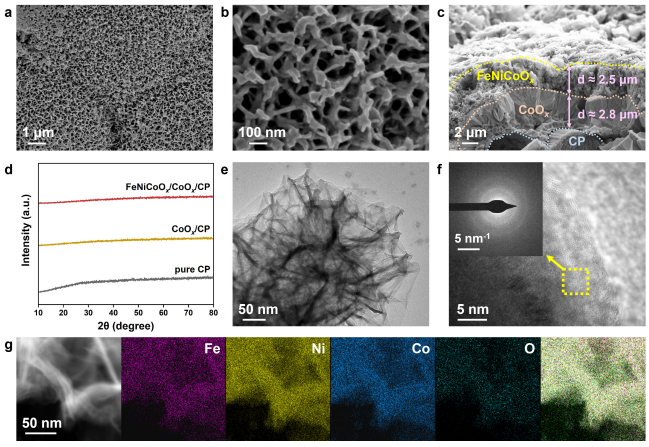

Figure 1. (a, b) FESEM images of $FeNiCoO_x/CoO_x/CP$ at different magnifications. (c) Cross-section SEM image of $FeNiCoO_x/CoO_x/CP$. (d) XRD patterns of $FeNiCoO_x/CoO_x/CP$, CoO_x/CP and pure CP. (e) TEM image of $FeNiCoO_x/CoO_x/CP$. (f) HRTEM image and SAED pattern (inset) of $FeNiCoO_x/CoO_x/CP$. (g) HAADF-STEM image and corresponding EDS elemental mapping images of $FeNiCoO_x/CoO_x/CP$.

The surface element composition and chemical state of samples were investigated through X-ray photoelectron spectroscopy (XPS). The XPS survey spectra(Figure S11a) further confirm the presence of Co and O on the surface of CoO_x, and Fe, Co, Ni and O on the surface of $FeNiCoO_x/CoO_x$. The deconvoluted high-resolution Fe 2p, Ni 2p, Co 2p and O 1s XPS spectra in Figure S11b–S11e demonstrate the existence of oxide states of all metal elements. Specifically, peaks located at 712.1 eV and 714.3 eV can be ascribed to Fe^{2+} 2p3/2 and Fe^{3+} 2p3/2 states, respectively (Figure S11b). Similarly, the binding energies of 855.9 eV and 857.1 eV correspond to 2p3/2 orbitals of Ni^{2+} and Ni^{3+}, respectively (Figure S11c). Co 2p XPS spectra could be deconvoluted into the characteristic peaks of Co^{2+} 2p3/2 (780.9 eV) and Co^{2+} 2p3/2 (792.7 eV) (Figure S11d). No shift could be observed in Co 2p peak positions between CoO_x and $FeNiCoO_x/CoO_x$. However, owing to the introduction of Fe and Ni, more Co^{2+} and less Co^{3+} exist in $FeNiCoO_x/CoO_x$ compared to CoO_x, suggesting that partial oxidation of Co may occur. The O 1s XPS spectra (Figure S11e) exhibit prominent M-O peaks at 529.3 eV, accompanied by peaks at 531.2 eV related to oxygen vacancy. The amount of oxygen vacancies dramatically

increased after the formation of $FeNiCoO_x$ layer, attributed to the reductive $Na_2S_2O_3$ ingredients. Quantitative analysis of XPS results was shown in Figure S11f and Table S1. The surface composition of Fe, Ni, and Co is found to be around 1:1:1, while the metal-to-oxygen concentration ratio approximates to be 3:4. The concentration of oxygen vacancies was further determined using electron paramagnetic resonance (EPR). As shown in Figure S12, the content of oxygen vacancies for $FeNiCoO_x/CoO_x$ is much higher than that for CoO_x, being consistent with XPS results.

Oxygen evolution reaction (OER) activity of the samples and commercial RuO_2/CP were evaluated in 1 M KOH electrolyte using three-electrode system. As depicted in Figure 2a, $FeNiCoO_x/CoO_x$/CP requires a low overpotential of 221 mV to reach 100 mA cm^{-2} (with 50% *i*R compensation), which not only surpasses $NiCoO_x/CoO_x$/CP (289 mV), $FeCoO_x/CoO_x$/CP (395 mV) and CoO_x/CP (404 mV) but also is superior to commercial RuO_2/CP (378 mV) across all ranges. The reaction kinetics of catalysts was assessed based on Tafel plots. As illustrated in Figure 2b, $FeNiCoO_x/CoO_x$/CP exhibited a Tafel slope of 30 mV dec^{-1}, significantly lower than those of $NiCoO_x/CoO_x$/CP (63 mV dec^{-1}), $FeCoO_x/CoO_x$/CP (82 mV dec^{-1}), CoOx/CP (167 mV dec^{-1}) and commercial RuO_2/CP (72 mV dec^{-1}). The OER electrocatalytic performance of the as-prepared $FeNiCoO_x/CoO_x$/CP is also better than those of previously reported non-noble-metal-based amorphous electrocatalysts (Figure 2c and Table S3).[46–58] Faradaic efficiency (FE) of $FeNiCoO_x/CoO_x$/CP was examined to evaluate the selectivity in OER. The evolution of O_2 gas over time under constant current was quantified. As shown in Figure 2d and Table S4, FE of $FeNiCoO_x/CoO_x$/CP is determined to be 98.47%, indicating the excellent selectivity of $FeNiCoO_x/CoO_x$/CP with almost no side reactions. Electrical impedance spectroscopy (EIS) investigations (Figure S13e) suggest that $FeNiCoO_x/CoO_x$/CP catalyst demonstrates the lowest charge transfer resistance (R_{ct}) value of 1.63 Ω compared with $NiCoO_x/CoO_x$/CP (1.69 Ω), $FeCoO_x/CoO_x$/CP (1.76 Ω) and CoO_x/CP (1.97 Ω) catalysts, revealing its superior charge transfer capability, which may be related to the delocalized electronic state resulting from synergistic interaction among three different metals. The electrochemical active surface area (ECSA) being proportion to the number of active sites was also assessed by measuring electrochemical double-layer capacitance (C_{dl}) (Figure S14). As depicted in Figure 2e, $FeNiCoO_x/CoO_x$/CP presented highest C_{dl} of 58.39 mF cm^{-2} in comparison of $NiCoO_x/CoO_x$/CP (42.58 mF cm^{-2}), $FeCoO_x/CoO_x$/CP (39.08 mF cm^{-2}), CoO_x/CP (12.57 mF cm^{-2}) and CP (2.15 mF cm^{-2}), implying more exposure of active sites.

Stability is another crucial parameter to evaluate practical application potential of catalysts. The chronoamperometry measurement was conducted at the overpotential of 250 mV, as shown in Figure 2f. $FeNiCoO_x/CoO_x$/CP catalyst exhibits negligible degradation after continuous operation up to 240 hours, indicating its exceptional electrochemical stability. The LSV curves before and after the chronoamperometry test also verify its remarkable stability (Figure S15a). Notably, the overpotential at 100 mA cm^{-2} increases by only 4 mV after the stability test. Moreover, the 3D network morphology and amorphous structure are well maintained (Figure S15b–d), further demonstrating its exceptional structural robustness. Figure S13f shows the multi-step chronopotentiometry for $FeNiCoO_x/CoO_x$/CP. All the voltage signals respond quickly and subsequently be stable for 4 hours when the current densities switch from 10 to 300 mA cm^{-2} followed by a return to 10 mA cm^{-2}, demonstrating its excellent stability at different densities. Note that when the current density returns to initial value of 10 mA cm^{-2}, negligible voltage difference could be observed, indicating the outstanding mass transfer performance and mechanical robustness of the $FeNiCoO_x/CoO_x$/CP electrode.

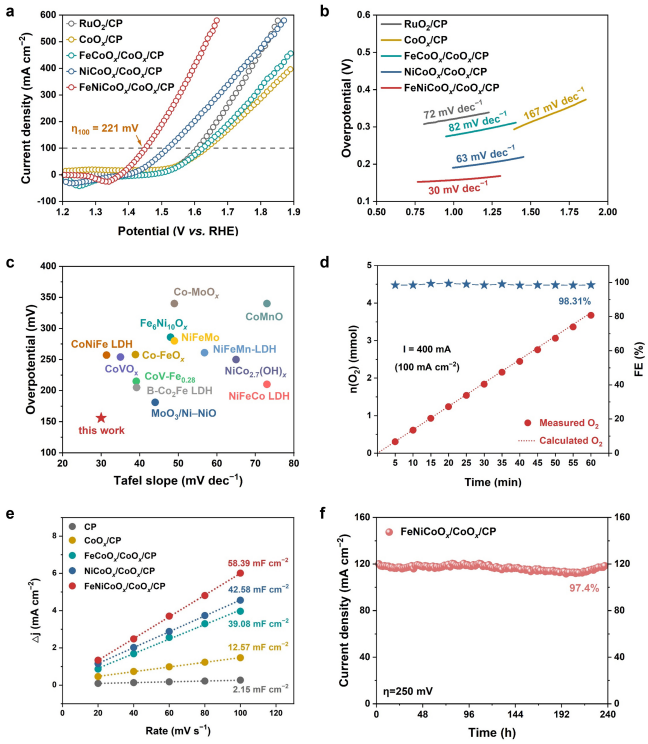

Figure 2. Electrocatalytic measurements of commercial RuO_2/CP, CoO_x/CP, $FeCoO_x/CoO_x$/CP, $NiCoO_x/CoO_x$/CP and $FeNiCoO_x/CoO_x$/CP for OER in 1 M KOH solution at 25 °C: (a) LSV curves with 50% iR compensation and (b) Tafel plots. (c) Comparisons of overpotential at 10 mA cm^{-2} and Tafel slope of $FeNiCoO_x/CoO_x$/CP with other recently reported amorphous catalysts. (d) Faradaic efficiency of $FeNiCoO_x/CoO_x$/CP for 60 minutes. (e) Variations of double-layer charging current as a function of scanning rates. (f) *i-t* curve of $FeNiCoO_x/CoO_x$/CP for 240 hours at the overpotential of 250 mV.

To elucidate the effect of amorphous structure on electrocatalytic activity, $FeNiCoO_x/CoO_x$/CP and CoO_x/CP were annealed at 600 °C, forming a crystalline structure (named as $FeNiCoO_4/Co_3O_4$/CP and Co_3O_4/CP) (Figure S16). During the process, numerous particles aggregate together, forming irregular chunks to bury plenty of active sites. Moreover, EPR analyses reveal that the concentration of oxygen vacancy decreases after annealing, attributed to partial oxidation. The crystalline $FeNiCoO_4/Co_3O_4$/CP exhibits an overpotential of 307 mV at 100 mA cm^{-2} and a Tafel slope of 94 mV dec^{-1}, inferior to those of $FeNiCoO_x/CoO_x$/CP (Figure S17a and S17b). R_{ct} value of $FeNiCoO_x/CoO_x$/CP is also lower than that of $FeNiCoO_4/Co_3O_4$/CP, suggesting that disordered amorphous structure facilitates charge transfer

better than ordered crystal structure. Lower C_{dl} value of $FeNiCoO_4/Co_3O_4$/CP (28.03 mF cm^{-2}) implying fewer active sites. After 48-hour stability test, only 85.4% initial current density could be preserved for $FeNiCoO_4/Co_3O_4$/CP, whereas the current density of $FeNiCoO_x/CoO_x$/CP remains unchanged, suggesting better stability of amorphous structure (Figure S17e). Additionally, EPR results reveal a reduction of oxygen vacancy concentration in $FeNiCoO_4/Co_3O_4$/CP after the OER operation. These results demonstrate that amorphous structure is benefit to the exposure and maintenance of active sites in the catalyst.

Samples with different concentrations of oxygen vacancies were synthesized by varying the addition of reductant $Na_2S_2O_3$ (denoted as $FeNiCoO_x/CoO_x$/CP-20 mmol, $FeNiCoO_x/CoO_x$/CP-10 mmol and $FeNiCoO_x/CoO_x$/CP-5 mmol). EPR spectra of as-prepared samples (Figure S18a) confirm successful control in the concentration of oxygen vacancy. Subsequently, the surface redox chemistry of $FeNiCoO_x/CoO_x$/CP-20 mmol , $FeNiCoO_x/CoO_x$/CP-10 mmol and $FeNiCoO_x/CoO_x$/CP-5 mmol were activated through CV tests. As revealed by CV curves, distinct oxidation peaks at approximately 1.41 V were observed during the anodic sweep, associated with self-surface reconstruction in electrochemical activation process (Figure S18b).[59] As the concentration of oxygen vacancies increases, the oxidation peak exhibits a negative shift, indicating lower external energy required to activate.[60] Moreover, the integrated area of anodic peak of CV curve for FeNiCoOx/CoOx/CP-20 mmol is significantly larger than those for FeNiCoOx/CoOx/CP-5 mmol and FeNiCoOx/CoOx/CP-10 mmol, demonstrating more active sites at the surface.[61] Consequently, the presence of oxygen vacancies facilities both kinetic and thermodynamic oxidative reconfiguration process.

The X-ray absorption near-edge spectroscopy (XANES) was employed to investigate the electronic structures of Fe, Ni and Co in $FeNiCoO_x/CoO_x$/CP before and after OER process. Figure 3a shows spectra lines consisting of Fe L_3-edge region ranging from 707 to 715 eV and Fe L_2-edge region ranging from 720 to 726 eV. It is reported that the intensity ratio of two peaks in L_2-edge serves as a reliable indicator to determine oxidation state of the detected element.[62] After normalizing the peak at 723.3 eV, it is evident that peak intensity of $FeNiCoO_x/CoO_x$/CP at 721.5 eV after OER process decreases, indicating a reduction in relative content of Fe^{2+}. Similarly, in Ni L-edge spectra (Figure 3b), peak intensity of $FeNiCoO_x/CoO_x$/CP at 879.9 eV after OER process is significantly lower, illustrating a decline in Ni^{2+} content. Co L-edge spectra in Figure 3c consist of two distinct regions: L_3-edge at around780 eV and L_2-edge at approximate 793 eV, attributed to spin-orbital splitting of Co 2p core hole. After OER process, a positive shift is observed, owing to an increase in oxidation state of Co. XPS measurements were also conducted to analyze the changes of chemical state for $FeNiCoO_x/CoO_x$/CP electrocatalyst. In the high-resolution Fe 2p XPS spectra (Figure S19b), the decreased Fe^{2+} proportion indicating elevated oxidation state of Fe, which is consistent with the result obtained from NEXAFS analysis. For Ni 2p and Co 2p XPS spectra, similar phenomena are also observed (Figure S19c and S19d). The increased oxidation states of metals owing to surface reconstruction, which are believed to significantly enhance OER activity. In O 1s spectra (Figure 3d), a distinct peak at 530.8 eV emerges after OER process, indicating the formation of hydroxyl.[63,64] A small negative shifts appear for all three metals, while a positive shift is observed for O element. The increase in electron density surrounding metal atoms and a corresponding decrease in electron density around O atoms suggest the electron transfer from oxygen to metal species. The EPR spectra, Raman spectra and XPS spectra characterizations after long-term stability test further confirm the reconstruction of the catalyst (Figure S20).

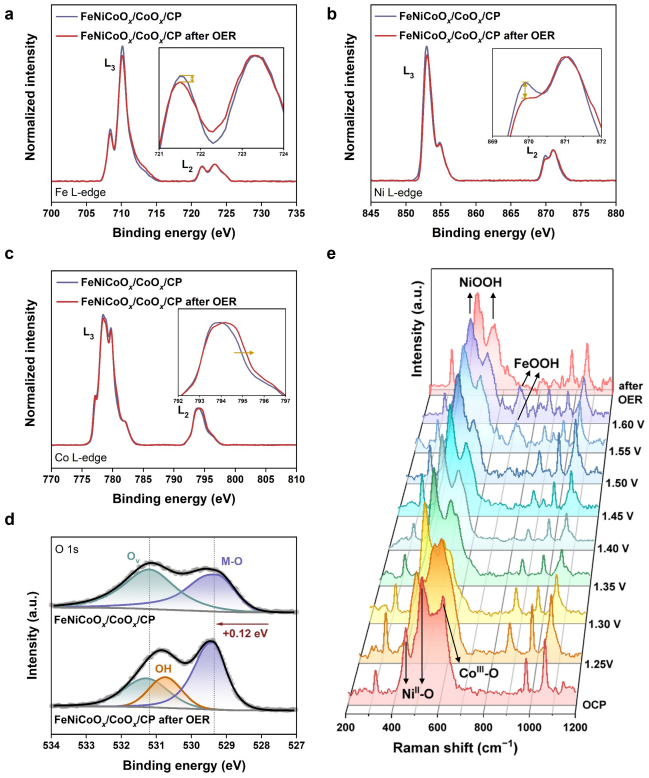

Figure 3. NEXAFS spectra of $FeNiCoO_x/CoO_x$/CP catalyst before and after OER test of: (a) Fe L-edge, (b) Ni L-edge and (c) Co L-edge. (d) XPS spectra of $FeNiCoO_x/CoO_x$/CP catalyst before and after OER test of O 1s. (e) In situ Raman spectra of $FeNiCoO_x/CoO_x$/CP under increasing potential from 1.25 to 1.60 V (vs. RHE).

To further monitor active phase and dynamic surface reconstruction throughout OER process, we have conducted in-situ Raman spectroscopy measurement.[65] As shown in Figure 3e, at open circuit potential (OCP), the catalyst exhibits characteristic peaks at 453 and 527 cm^{-1} corresponding to Ni^{II}-O and characteristic peak at 615 cm^{-1} corresponding to Co^{III}-O.[66] Upon exceeding a potential of 1.25 V, reconstruction occurs. When the voltage surpasses 1.30 V, observed frequencies of 469 and 557 cm^{-1} correspond well to E_g bending and A_{1g} stretching vibrations of Ni^{III}-O in γ-NiOOH, respectively.[67,68] When the voltage reaches 1.5 V, characteristic peak of β-FeOOH emerges at 714 cm^{-1}, exhibiting an enhanced intensity proportional to applied voltage increment.[69,70] Both FeOOH and NiOOH are formed as voltage rising, whereas NiOOH is initially generated. Furthermore, only NiOOH peaks was observed after OER test. Consequently, in-situ activated NiOOH is more likely to function as authentic active species during OER process.

To obtain insights into catalytic mechanism, density functional theory (DFT) calculations combined with Hubbard U

(DFT + U) approach were implemented.[71] Figure 4a exhibits four-step OER pathway proposed by Nørskov et al.[72] The adsorption configurations of the OER-involved intermediate species for all computed models are shown in Figure S21. The calculated Gibbs free energies (ΔG) of each step involved for all structural models at U = 0 V vs. RHE and U = 1.23 V vs. RHE are presented in Figure 4b and Figure S22a–S22c. When Ni is active site, rate-determining step (RDS) is the transformation of OH* into O* (step II). The introduction of Fe and Co results in lower energy of O* species, leading to lower Gibbs energy required. This can be attributed to synergistic compositions that stabilize O* intermediate species. ΔG value of OER process on Ni active site for FeNiCoOOH is 0.307 eV, lower than those for NiCoOOH (0.880 eV) and NiOOH (1.065 eV). The low ΔG manifests a decreased energy barrier, thereby enhancing OER performance. While for models with Fe active site, RDS is the transformation of O* into OOH* (step III). The substantial decrease in Gibbs free energies of FeNiCoOOH and FeCoOOH compared to FeOOH also verifies the synergistic effect among metal elements. It is noteworthy that in the same FeNiCoOOH model, the Ni active site exhibits a lower barrier than Fe site, indicating that it may be the active site. This calculation conclusion is in accordance with the results obtained from in-situ Raman analysis.

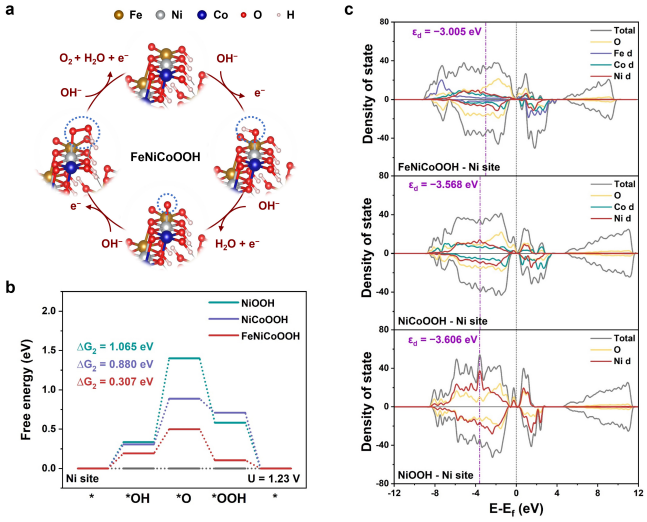

Figure 4. (a) Schematic diagram of OER process. (b) Free-energy diagram for the four steps of OER at 1.23 V of Ni site in NiOOH, NiCoOOH and FeNiCoOOH. (c) PDOS for Ni sites in FeNiCoOOH, NiCoOOH and NiOOH.

The electronic structures of Ni and Fe sites in the models were further investigated through density of states (DOS) (Figure 4c and Figure S22d-S22f). An evident disparity in projected density of states (PDOS) plots between spin-up and spin-down electrons can be observed, suggesting that all metal atoms are in spin-polarized states. With the up-shifting of d-band center to Fermi level, it is more effective to modulate electronic structure of metal sites which contain more anti-bonding states and higher valence states, anticipated to enhance OER activity. With d-band center being closest to Fermi level, Ni sites in FeNiCoOOH demonstrate superior catalytic performance. The band structures of NiOOH and FeCoNiOOH were also represented in Figure S23. A small band gap exists between valence band maxima (VBM) and conduction band minima (CBM) of NiOOH and Fermi level is located inside the gap between CBM and VBM. For FeCoNiOOH, there is no appreciable band gap, indicating that it holds metal-like properties with significant conductivity and efficient charge transportation.

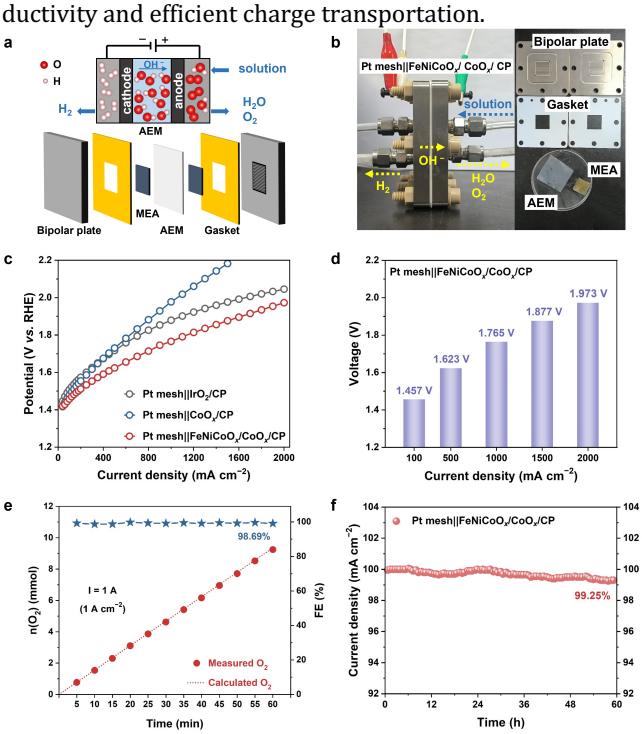

Figure 5. (a) Schematic diagrams of AEMWE. (b) Photographs of AEMWE. (c) Polarization curves of AEMWE with different electrocatalysts in 1 M KOH at 60 °C. (d) Cell voltages at different current densities. (e) Faradaic efficiency of $FeNiCoO_x/CoO_x$/CP-assembled AEMWE for 60 minutes. (f) Durability test at 100 mA cm^{-2} up to 60 hours for $FeNiCoO_x/CoO_x$/CP-assembled AEMWE.

The as-developed catalyst coupling with Pt/C shows good performance (1.584 V @ 100 mA cm^{-2}) and stability for overall water splitting (Figure S24). Furthermore, a real anion-exchange-membrane water electrolyzer (AEMWE) with the $FeNiCoO_x/CoO_x$/CP used as anode OER catalyst and Pt mesh employed as cathode HER catalyst (Figure 5a and 5b). CoO_x/CP and commercial IrO_2/CP-based AEMWEs were also assembled for comparison. The polarization curves of the AEMWE devices with different electrocatalysts are depicted in Figure 5c. Impressively, $FeNiCoO_x/CoO_x$/CP-assembled electrolyzer could afford a current density of 1 A cm^{-2} at a cell voltage of 1.765 V at 60 °C in 1 M KOH solution without *i*R compensation (Figure 5d), which is superior to those of IrO_2/CP (1.879 V) and most previously reported AEMWE (Figure S25a and Table S8). The Faradaic efficiency of $FeNiCoO_x/CoO_x$/CP-assembled AEMWE device was examined to be 98.69% (Figure 5e and Table S9), suggesting a high selectivity. Moreover, the device exhibits negligible performance degradation over a duration of 60 hours throughout continuous operation under constant current density of 100 mA cm^{-2} (Figure 5f), indicating an excellent stability of the $FeNiCoO_x/CoO_x$/CP anode in practical electrolyzer. Figure S25c shows the polarization curves before and after stability test, further verifying its remarkable stability.

In summary, we developed a facile method to fabricate amorphous trinary metal oxide $FeNiCoO_x/CoO_x$/CP with

abundant oxygen vacancies. The interaction among Fe, Ni and Co components not only facilitates electron transfer process but also optimizes adsorption energy of intermediates, while amorphous structures and abundant oxygen vacancies are benefit to the exposure of active sites. Accordingly, the as-synthesized $FeNiCoO_x/CoO_x$/CP catalyst exhibits an exceptional performance in alkaline solution, achieving a current density of 100 mA cm^{-2} at a low overpotential of 221 mV as well as a remarkable long-term stability. More importantly, the $FeNiCoO_x/CoO_x$/CP-assembled AEMWE could afford a current density of 1 A cm^{-2} at a low voltage of 1.765 V, demonstrating its significant practical application potential. The findings in this work may pave a new avenue for the rational design of high-performance OER electrocatalyst based on earth-abundant transition metals.

ASSOCIATED CONTENT

Supporting Information. Experimental section including catalyst preparation, characterization, electrochemical measurements, AEMWE assembly and measurements, and computational method; schematic of synthetic process; additional SEM images; BET measurements; zeta potential tests; contact angle measurement; additional XRD patterns; additional TEM images and SAED pattern; EDS image and spectrum; XPS spectra; additional electrochemical measurements; EPR spectra; optimized structures for all intermediates adsorbed on metal sites; free-energy diagrams and projected density of states; band structure diagrams; elements contents measured by XPS; comparisons of OER and AEMWE performances; detailed data in Faraday efficient measurements; calculated Gibbs free energy for molecules and intermediate in OER; calculated Gibbs free energy for OER process. (PDF) This material is available free of charge via the Internet at http://pubs.acs.org.

AUTHOR INFORMATION

Corresponding Author

Renbing Wu – Department of Materials Science, Fudan University, Shanghai 200438, China; orcid.org/0000-0003-2815-2797; Email: rbwu@fudan.edu.cn

Yanhui Guo – Department of Materials Science, Fudan University, Shanghai 200433, China; orcid.org/0000-0002-7477-5234; Email: gyh@fudan.edu.cn

Author

Qianyun Bai – Department of Materials Science, Fudan University, Shanghai 200438, China

Da Liu – Department of Materials Science, Fudan University, Shanghai 200438, China

Xiaoxiao Yan – Department of Materials Science, Fudan University, Shanghai 200438, China

Peifang Guo – Department of Materials Science, Fudan University, Shanghai 200438, China

Xingyu Ding – Department of Materials Science, Fudan University, Shanghai 200438, China

Kang Xiang – Department of Materials Science, Fudan University, Shanghai 200438, China

Xin Tu – Department of Electrical Engineering and Electronics, University of Liverpool, Liverpool L69 3GJ, UK

Notes

The authors declare no competing financial interest.

ACKNOWLEDGMENT

This work was financially supported by National Natural Science Foundation of China (Nos. 52071084 and 52225104), "Shuguang Program" supported by Shanghai Education Development Foundation and Shanghai Municipal Education Commission (20SG03), and Science and Technology Commission of Shanghai Municipality (No. 22520710600).

REFERENCES

(1) Feng, C.; Faheem, M. B.; Fu, J.; Xiao, Y. Q.; Li, C. L.; Li, Y. B. Fe-based Electrocatalysts for Oxygen Evolution Reaction: Progress and Perspectives. *ACS Catal.* 2020, 10(7), 4019-4047.

(2) Guo, P. F.; Liu, D. Wu, R. B, Recent Progress in Design Strategy of Anode for Seawater Electrocatalysis, *Small Struct.*, 2023, 4, 2300192.

(3) Yu, Z. Y.; Duan, Y.; Feng, X. Y.; Yu, X. X.; Gao, M. R.; Yu, S. H. Clean and Affordable Hydrogen Fuel from Alkaline Water Splitting: Past, Recent Progress, and Future Prospects. *Adv. Mater.* 2021, 33(31), 2207100.

(4) Zhou, A. Q.; Yang, J. M.; Zhu, X. W.; Zhu, X. L.; Liu, J. Y.; Zhong, K.; Chen, H. X.; Chu, J. Y.; Du, Y. S.; Song, Y. H.; Qian, J. C.; Li, H. M.; Xu, H. Self-assembly Construction of NiCo LDH/ultrathin g-C_3N_4 Nanosheets Photocatalyst for Enhanced CO_2 Reduction and Charge Separation Mechanism Study. *Rare Metal.* 2022, 41(6), 2118-2128.

(5) Wang, X. P.; Zhong, H. Y.; Xi, S. B.; Lee, W. S. V.; Xue, J. M. Understanding of Oxygen Redox in the Oxygen Evolution Reaction. *Adv. Mater.* 2022, 34(50), 2107956.

(6) Cheng, W. J.; Wang, H.; Gu, Z. Y.; Cao, M.; He, C. C.; Li, J.; Li, Z.; Tian, L. Modulation of the Electronic Structure of CoP by Surface and Interface Codoping Boosts Electrocatalytic Oxygen Evolution Reaction. *Int. J. Hydrogen Energy* 2021, 51, 914-921.

(7) Qiu, H. J.; Fang, G.; Gao, J. J.; Wen, Y. R.; Lv, J.; Li, H. L.; Xie, G. Q.; Liu, X. J.; Sun, S. H. Noble Metal-free Nanoporous High-entropy Alloys as Highly Efficient Electrocatalysts for Oxygen Evolution Reaction. *ACS Mater. Lett.* 2019, 1(5), 526-533.

(8) Liu, D.; Yan, X. X.; Guo, P. F.; Yang, Y. X.; He, Y. F.; Liu, J.; Chen, J.; Pan, H. G.; Wu, R. B. Inert Mg Incorporation to Break the Activity/Stability Relationship in High-entropy Layered Hydroxides for the Electrocatalytic Oxygen Evolution Reaction. *ACS Catal.* 2023, 13(11), 7698-7706.

(9) Li, Z.; Sun, L. M.; Zhang, Y.; Han, Y. L.; Zhuang, W. C.; Tian, L.; Tan. W. Y. Coupled and Decoupled Electrochemical Water Splitting for Boosting Hydrogen Evolution: A Review and Perspective. *Coordin. Chem. Rev.* 2024, 510, 215837.

(10) Xie, X. H.; Du, L.; Yon, L. T.; Park, S. Y.; Qiu, Y.; Sokolowski, J.; Wang, W.; Shao, Y. Y. Oxygen Evolution Reaction in Alkaline Environment: Material Challenges and Solutions. *Adv. Funct. Mater.* 2022, 32(21), 2110036.

(11) Zhang, K. X.; Zou, R. Q. Advanced Transition Metal-based OER Electrocatalysts: Current Status, Opportunities, and Challenges. *Small* 2021, 17(37), 2100129.

(12) Yuan, C. Z.; Hui, K. S.; Yin, H.; Zhu, S. Q.; Zhang, J. T.; Wu, X. L.; Hong, X. T.; Zhou, W.; Fan, X.; Bin, F.; Chen, F. M.; Hui, K. N. Regulating Intrinsic Electronic Structures of Transition-metal-based Catalysts and the Potential Applications for Electrocatalytic Water Splitting. *ACS Mater. Lett.* 2021, 3(6), 752-780.

(13) Li, W.; Liu, J.; Guo, P. F.; Li, H. Z.; Fei, B.; Guo, Y. H.; Pan, H. G.; Sun, D. L.; Fang, F.; Wu, R. B. Co/CoP Heterojunction on Hierarchically Ordered Porous Carbon as a Highly Efficient Electrocatalyst

for Hydrogen and Oxygen Evolution. *Adv. Energy Mater.* 2021, 11(42), 2102134.

(14) Zhang, R. R.; Pan, L.; Guo, B. B.; Huang, Z. F.; Chen, Z. X.; Wang, L.; Zhang, X. W.; Guo, Z. Y.; Xu, W.; Loh, K. P.; Zou, J. J. Tracking the Role of Defect Types in Co_3O_4 Structural Evolution and Active Motifs during Oxygen Evolution Reaction. *J. Am. Chem. Soc.* 2023, 145(4), 2271–2281.

(15) Chakraborty, B.; Beltrán-Suito, R.; Hausmann, J. N.; Garai, S.; Driess, M.; Menezes, P. W. Enabling Iron-based Highly Effective Electrochemical Water-splitting and Selective Oxygenation of Organic Substrates through In Situ Surface Modification of Intermetallic Iron Stannide Precatalyst. *Adv. Energy Mater.* 2020, 10(30), 2001377.

(16) Zhang, Y.; Du, M. M.; Ma, Y. X.; Shang, J.; Qiu, B. C. Valence Engineering via Double Exchange Interaction in Spinel Oxides for Enhanced Oxygen Evolution Catalysis. *Mater. Today Catal.* 2023, 3, 100027.

(17) Wang, D.; Chang, Y. X.; Li, Y. R.; Zhang, S. L.; Xu, S. L. Well-dispersed $NiCoS_2$ Nanoparticles/rGO Composite with a Large Specific Surface Area as an Oxygen Evolution Reaction Electrocatalyst. *Rare Met.* 2021, 40(11), 3156-3165.

(18) Guo, P. F.; Shi, L. X.; Liu, D.; Wang, X. Q.; Gao, F.; Ha, Y.; Yin, J.; Liu, M.; Pan, H. G.; Wu, R. B. Fe-doping-induced Cation Substitution and Anion Vacancies Promoting Co_3O_4 Hexagonal Nanosheets for Efficient Overall Water Splitting. *Mater. Today Catal.* 2023, 1, 100002.

(19) Lei, X.; Tang, Q. Y.; Zheng, Y. P.; Kidkhunthod, P.; Zhou, X. L.; Ji, B. F.; Tang, Y. B. High-entropy Single-atom Activated Carbon Catalysts for Sustainable Oxygen Electrocatalysis. *Nat. Sustain.* 2023, 6(7), 816-826.

(20) Han, J. Y.; Guan, J. Q.; Multicomponent Transition Metal Oxides and (Oxy)hydroxides for Oxygen Evolution. *Nano Res.* 2023, 16(2), 1913-1966.

(21) Song, J. J.; Wei, C.; Huang, Z. F.; Liu, C. T.; Zeng, L.; Wang, X.; Xu, Z. C. J. A Review on Fundamentals for Designing Oxygen Evolution Electrocatalysts. *Chem. Soc. Rev.* 2020, 49(7), 2196-2214.

(22) Fei, B.; Chen, Z. L.; Ha, Y.; Wang, R. R.; Yang, H. Y.; Xu, H. B.; Wu, R. B, Anion-Cation Co-Substitution Activation of Spinel $CoMoO_4$ for Efficient Oxygen Evolution Reaction, Chem. Eng. J. 2020, 394, 124926.

(23) Wang, W.; Wang, Z. X.; Hu, Y. C.; Liu. Y. C.; Chen, S. L. A Potential-driven Switch of Activity Promotion Mode for the Oxygen Evolution Reaction at Co_3O_4/NiO_xH_y Interface. *eScience* 2022, 2, 438-444.

(24) Wei, C. Y.; Heng, N. N.; Wang, Z. H.; Song, X. S.; Sun, Z. X.; Zhu, X. B.; He, J. L.; Zhao, Y.; Wang, X. B. Dynamic Active Site Evolution and Stabilization of Core-shell Structure Electrode for Oxygen Evolution Reaction. *Chem. Eng. J.* 2022, 435, 134672.

(25) Cai, W. Z.; Yang, H. B.; Zhang, J. M.; Chen, H. C.; Tao, H. B.; Gao, J. J.; Liu, S.; Liu, W.; Li, X. N.; Liu, B. Amorphous Multimetal Alloy Oxygen Evolving Catalysts. *ACS Mater. Lett.* 2020, 2(6), 624-631.

(26) Duan, Y.; Sun, S. N.; Sun, Y. M.; Xi, S. B.; Chi, X.; Zhang, Q. H.; Ren, X.; Wang, J. X.; Ong, S. J. H.; Du, Y. H.; Gu, L.; Grimaud, A.; Xu, Z. C. J. Mastering Surface Reconstruction of Metastable Spinel Oxides for Better Water Oxidation. *Adv. Mater.* 2019, 31(12), 1807898.

(27) Antink, W. H.; Lee, S. B.; Lee, H. S.; Shin, H.; Yoo, T. Y.; Ko, W. J.; Shim, J.; Na, G. M.; Sung, Y. E.; Hyeon, T. High-valence Metal-driven Electronic Modulation for Boosting Oxygen Evolution Reaction in High-entropy Spinel Oxide. *Adv. Funct. Mater.* 2024, 34(1), 2309428.

(28) Yan, D. F.; Xia, C. F.; Zhang, W. J.; Hu, Q.; He, C. X.; Xia, B. Y.; Wang, S. Y. Cation Defect Engineering of Transition Metal Electrocatalysts for Oxygen Evolution Reaction. *Adv. Energy Mater.* 2022, 12(45), 2202317.

(29) Luo, X. Y.; Zheng, H.; Lai, W. D.; Yuan, P.; Li, S. W.; Li, D.; Chen, Y. Defect Engineering of Carbons for Energy Conversion and Storage Applications. *Energy Environ. Mater.* 2023, 6(3), DOI:10.1002/eem2.12402.

(30) Zhang, L. J.; Jang, H.; Liu, H. H.; Kim, M. G.; Yang, D. J.; Liu, S. G.; Liu, X. E.; Cho, J. Sodium-decorated Amorphous/Crystalline RuO_2 with Rich Oxygen Vacancies: A Robust pH-universal Oxygen Evolution Electrocatalyst. *Angew. Chem. Int. Ed.* 2021, 60(34), 18821-18829.

(31) Chen, Z. L.; Chen, M.; Yan, X. X.; Jia, H. X.; Fei, B.; Ha, Y.; Qing, H. L.; Yang, H. Y.; Liu, M.; Wu, R. B. Vacancy Occupation-Driven Structural Transition in $CoTe_2$ for Boosted Oxygen Evolution Reaction, *ACS Nano*, 2020, 14, 6968–6979.

(32) Kang, T.; Kim, J. Optimal Cobalt-based Catalyst Containing High-ratio of Oxygen Vacancy Synthesized from Metal-organic-framework (MOF) for Oxygen Evolution Reaction (OER) Enhancement. *Appl. Surf. Sci.* 2021, 560, 150035.

(33) Li, J.; Yang, F.; Du, Y. Z.; Jiang, M.; Cai, X. Y.; Hu, Q. D.; Zhang, J. The Critical Role of A,B-site Cations and Oxygen Vacancies on the OER Electrocatalytic Performances of $Bi_{0.15}Sr_{0.85}Co_{1-x}Fe_xO_{3-\delta}$ ($0.2 \leq x \leq 1$) Perovskites in Alkaline Media. *Chem. Eng. J.* 2023, 451, 138646.

(34) Xu, H. B.; Fei, B.; Cai, G. H.; Ha, Y.; Liu, J.; Jia, H. X.; Zhang, J. C.; Liu, M.; Wu, R. B. Boronization-Induced Ultrathin 2D Nanosheets with Abundant Crystalline-Amorphous Phase Boundary Supported on Nickel Foam Toward Efficient Water Splitting, *Adv. Energy Mater*., 2020, 10, 1902714.

(35) Guo, T. Q.; Li, L. D.; Wang, Z. C. Recent Development and Future Perspectives of Amorphous Transition Metal-based Electrocatalysts for Oxygen Evolution Reaction. *Adv. Energy Mater.* 2022, 12(24), 2200827.

(36) Li, D. Y.; Xiang, R.; Yu, F.; Zeng, J. S.; Zhang, Y.; Zhou, W. C.; Liao, L. L.; Zhang, Y.; Tang, D. S.; Zhou, H. Q. In Situ Regulating Cobalt/Iron Oxide-oxyhydroxide Exchange by Dynamic Iron Incorporation for Robust Oxygen Evolution at Large Current Density. *Adv. Mater.* 2023, 36(5). 2305685.

(37) Lv, J. J.; Wang, L. M.; Li, R. S.; Zhang, K. Y.; Zhao, D. F.; Li, Y. Q.; Li, X. J.; Huang, X. B.; Wang, G. Constructing a Hetero-interface Composed of Oxygen Vacancy-enriched Co_3O_4 and Crystalline-Amorphous NiFe-LDH for Oxygen Evolution Reaction. *ACS Catal.* 2021, 11(23), 14338-14351.

(38) Yang, H. Y.; Chen, Z. L.; Guo, P. F.; Fei, B.; Wu, R. B. B-doping-induced Amorphization of LDH for Large-current-density Hydrogen Evolution Reaction. *Appl. Catal. B: Environ.* 2020, 261, 118240.

(39) Bai, Q. Y.; Yan, X. X.; Liu, D.; Xiang, K.; Tu, X.; Guo, Y. H.; Wu, R. B. Amorphous Quaternary Alloy Nanoplates for Efficient Catalysis of Hydrogen Evolution Reaction. *J. Alloys Compd.* 2024, 972, 172730.

(40) Li, X. Y.; Xiao, L. P.; Zhou, L.; Xu, Q. C.; Weng, J.; Xu, J.; Liu, B. Adaptive Bifunctional Electrocatalyst of Amorphous CoFe Oxide@2D Black Phosphorus for Overall Water Splitting. *Angew. Chem. Int. Ed.* 2020, 59(47), 21106-21113.

(41) Li, S. J.; Wang, H.; Ma, Z. M.; Xiao, Q. L.; Gao, Q.; Jiang, Y. M.; Shen, W.; He, R. X.; Li, M. Rapid Surface Reconstruction of Amorphous $Co(OH)_2/WO_x$ with Rich Oxygen Vacancies to Promote Oxygen Evolution. *Chemsuschem* 2021, 14(24), 5534-5540.

(42) Li, S. N.; Ma, P. L.; Yang, J. S.; Krishnan, S.; Kesavan, K. S.; Xing, R. M.; Liu, S. H. Facile Construction of Three-dimensional Heterostructured CuCo2S4 Bifunctional Catalyst for Alkaline Water Electrolysis. *Catalysts* 2023, 13(5), 13050881.

(43) Singh, T. I.; Maibam, A.; Cha, D. C.; Yoo, S.; Babarao, R.; Lee, S. U.; Lee, S. High-alkaline Water-splitting Activity of Mesoporous 3D Heterostructures: An Amorphous-shell@crystalline-core Nano-assembly of Co-Ni-phosphate Ultrathin-nanosheets and V-doped Cobalt-nitride Nanowires. *Adv. Sci.* 2022, 9(23), 2201311.

(44) Hu, F.; Yu, D. S.; Ye, M.; Wang, H.; Hao, Y. A.; Wang, L. Q.; Li, L. L.; Han, X. P.; Peng, S. J. Lattice-matching Formed Mesoporous Transition Metal Oxide Heterostructures Advance Water Splitting by Active Fe-O-Cu Bridges. *Adv. Energy Mater.* 2022, 12(19), 2200067.

(45) Gao, H. Q.; Sun, W.; Tian, X. L.; Liao, J. J.; Ma, C. L.; Hu, Y. L.; Du, G.; Yang, J.; Ge, C. J. Amorphous-amorphous Coupling Enhancing the Oxygen Evolution Reaction Activity and Stability of the NiFe-based Catalyst. *ACS Appl. Mater. Interfaces* 2022. 14(13), 15205-15213.

(46) Liardet, L.; Hu, X. L. Amorphous Cobalt Vanadium Oxide as a Highly Active Electrocatalyst for Oxygen Evolution. *ACS Catal.* 2019, 9(6), 5522.

(47) Guo, C. Y.; Sun, X.; Kuang, X.; Gao, L. F.; Zhao, M. Z.; Qu, L.; Zhang, Y.; Wu, D.; Ren, X.; Wei, Q. Amorphous Co-doped MoO_x Nanospheres with a Core-Shell Structure toward an Effective Oxygen Evolution Reaction. *J. Mater. Chem. A* 2019, 7(3), 1005-1012.

(48) Zhao, C. T.; Yu, C.; Huang, H. W.; Han, X. T.; Liu, Z. B.; Qiu, J. S. Co Ion-Intercalation Amorphous and Ultrathin Microstructure for High-Rate Oxygen Evolution. *Energy Storage Mater.* 2018, 10, 291-296.

(49) Lin, X. Q.; Li, X. Z.; Li, F.; Fang, Y. Y.; Tian, M.; An, X. C.; Fu, Y.; Jin, J.; Ma, J. T. Precious-Metal-Free Co-Fe-O_x Coupled Nitrogenen-Riched Porous Carbon Nanosheets Derived from Schiff-Base Porous Polymers as Superior Electrocatalysts for the Oxygen Evolution Reaction. *J. Mater. Chem. A* 2016, 4(17), 6505-6512.

(50) Duan, Y.; Yu, Z. Y.; Hu, S. J.; Zheng, X. S.; Zhang, C. T.; Ding, H. H.; Hu, B. C.; Fu, Q. Q.; Yu, Z. L.; Zheng, X.; Zhu, J. F.; Gao, M. R.; Yu, S. H. Scaled-Up Synthesis of Amorphous NiFeMo Oxides and Their Rapid Surface Reconstruction for Superior Oxygen Evolution Catalysis. *Angew. Chem. Int. Ed.* 2019, 58(44), 15772-15777.

(51) Cai, Z.; Li, L. D.; Zhang, Y. W.; Yang, Z.; Yang, J.; Guo, Y. J.; Guo, L. Amorphous Nanocages of Cu-Ni-Fe Hydr(oxy)oxide Prepared by Photocorrosion For Highly Efficient Oxygen Evolution. *Angew. Chem. Int. Ed.* 2019, 58, 4189-4194.

(52) Cai, Z.; Zhou, D. J.; Wang, M. Y.; Bak, S. M.; Wu, Y. S.; Wu, Z. S.; Tian, Y.; Xiong, X. Y.; Li, Y. P.; Liu, W.; Siahrostami, S.; Kuang, Y.; Yang, X. Q.; Duan, H. H.; Feng, Z. X.; Wang, H. L.; Sun, X. M. Introducing Fe^{2+} into Nickel-Iron Layered Double Hydroxide: Local Structure Modulated Water Oxidation Activity. *Angew. Chem. Int. Ed.* 2018, 57(30), 9392-9396.

(53) Kuang, M.; Zhang, J. M.; Liu, D. B.; Tan, H. T.; Dinh, K. N.; Yang, L.; Ren, H.; Huang, W. J.; Fang, W.; Yao, J. D.; Hao, X. D.; Xu, J. W.; Liu, C. T.; Song, L.; Liu, B.; Yan, Q. Y. Amorphous/Crystalline Heterostructured Cobalt-Vanadium-Iron (Oxy)hydroxides for Highly Efficient Oxygen Evolution Reaction. *Adv. Energy Mater.* 2020, 10(43), 2002215.

(54) Nai, J. W.; Yin, H. J.; You, T. T.; Zheng, L. R.; Zhang, J.; Wang, P. X.; Jin, Z.; Tian, Y.; Liu, J. Z.; Tang, Z. Y.; Guo, L. Efficient Electrocatalytic Water Oxidation by Using Amorphous Ni-Co Double Hydroxides Nanocages. *Adv. Energy Mater.* 2015, 5(10), 1401880.

(55) Babar, P.; Lokhande, A.; Karade, V.; Pawar, B.; Gang, M. G.; Pawar, S.; Kim, J. H. Bifunctional 2D Electrocatalysts of Transition Metal Hydroxide Nanosheet Arrays for Water Splitting and Urea Electrolysis. *ACS Sustain. Chem. Eng.* 2019, 7(11), 10035-10043.

(56) Liu, J. Z.; Hu, Q.; Wang, Y.; Yang, Z.; Fan, X. Y.; Liu, L. M.; Guo, L. Achieving Delafossite Analog by in Situ Electrochemical Self-Reconstruction as an Oxygen-Evolving Catalyst. *Proc. Natl. Acad. Sci.* 2020, 117(36), 21906-21913.

(57) Wu, J. S.; Yang, T.; Fu, R.; Zhou, M.; Xia, L. X.; Wang, Z. Y.; Zhao, Y. Constructing Electrocatalysts with Composition Gradient Distribution by Solubility Product Theory: Amorphous/Crystalline Co-NiFe-LDH Hollow Nanocages. *Adv. Funct. Mater.* 2023, 33(37), 2300808.

(58) Wang, X.; Zuo, Y.; Horta, S.; He, R.; Yang, L. L.; Moghaddam, A. O.; Ibáñez, M.; Qi, X. Q.; Cabot, A CoFeNiMnZnB as a High-Entropy Metal Boride to Boost the Oxygen Evolution Reaction. *ACS Appl. Mater. Interfaces* 2022, 14(42), 48212-48219.

(59) Li, Y. Y.; Du, X. C.; Huang, J. W.; Wu, C. Y.; Sun, Y. H.; Zou, G. F.; Yang, C. T.; Xiong, J. Recent Progress on Surface Reconstruction of Earth-abundant Electrocatalysts for Water Oxidation. Small 2019, 15(35), 1901980.

(60) Tsuji, E.; Imanishi, A.; Fukui, K.; Nakato, Y. Electrocatalytic Activity of Amorphous RuO2 Electrode for Oxygen Evolution in an Aqueous Solution. Electrochim. Acta 2011, 56(5), 2009-2016.

(61) Chen, G.; Zhu, Y. P.; Chen, H. M.; Hu, Z. W.; Hung, S. F.; Ma, N. N.; Dai, J.; Lin, H. J.; Chen, C. T.; Zhou, W.; Shao, Z. P. An Amorphous Nickel-iron-based Electrocatalyst with Unusual Local Structures for Ultrafast Oxygen Evolution Reaction. Adv. Mater. 2019, 31(28), 1900883.

(62) Shen, Z. C.; Qu, M.; Shi, J.; Oropeza, F. E.; O'Shea, V. A. D.; Gorni, G.; Tian, C. M.; Hofmann, J. P.; Cheng, J.; Li, J.; Zhang, K. H. L. Correlating the Electronic Structure of Perovskite $La_{1-x}Sr_xCoO_3$ with Activity for the Oxygen Evolution Reaction: The Critical Role of Co 3d Hole State. *J. Energy Chem.* 2022, 65, 637-645.

(63) Wang, X. Z.; Zhou, Y.; Luo, J. B.; Sun, F. C.; Zhang, J. Synthesis of V-doped Urchin-like $NiCo_2O_4$ with Rich Oxygen Vacancies for Electrocatalytic Oxygen Evolution Reactions. *Electrochim. Acta* 2022, 406, 139800.

(64) Li, Y. P.; Wang, W. T.; Cheng, M. Y.; Feng, Y. F.; Han, X.; Qian, Q. Z.; Zhu, Y.; Zhang, G. Q. Arming Ru with Oxygen-vacancy-enriched RuO_2 Sub-nanometer Skin Activates Superior Bifunctionality for pH-universal Overall Water Splitting. *Adv. Mater.* 2023, 35(24), 2206351.

(65) Li, Z.; Yang, H. M.; Cheng, W. J.; Tian, L. Recent Progress of In Situ/Operando Characterization Techniques for Electrocatalytic Energy Conversion reaction. *Chinese Chem. Lett.* DOI: 10.1016/j.cclet.2023.109237

(66) Gao, L.; Li, Y. W.; Li, G. F.; Huo, J. Q.; Jia, L. S. Interface Charge Induced Self-assembled $(Co(OH)_2)_4$@$La(OH)_3$ Heterojunction Derived from Co_4-MOF@$La(HCO_2)_3$ to Boost Oxygen Evolution Reaction. *Chem. Eng. J.* 2023, 451, 138743.

(67) Zhai, P. L.; Wang, C.; Zhao, Y. Y.; Zhang, Y. X.; Gao, J. F.; Sun, L. C.; Hou, J. A. Regulating Electronic States of Nitride/Hydroxide to Accelerate Kinetics for Oxygen Evolution at Large Current Density. *Nat. Commun.* 2023, 14(1), 1873.

(68) Lee, S.; Bai, L. C.; Jeong, J.; Stenzel, D.; Schweidler, S.; Breitung, B. High Entropy Molybdate-derived FeOOH Catalyzes Oxygen Evolution Reaction in Alkaline Media. *Electrochim. Acta* 2023, 463, 142775.

(69) Wei, B. B.; Shang, C. Q.; Wang, X.; Zhou, G. F. Conductive FeOOH as Multifunctional Interlayer for Superior Lithium-sulfur Batteries. *Small* 2020, 16(34), 2002789.

(70) Nieuwoudt, M. K.; Comins, J. D.; Cukrowski, I. The Growth of the Passive Film on Iron in 0.05 M NaOH Studied in Situ by Raman Micro-spectroscopy and Electrochemical Polarisation. Part I: Near-resonance Enhancement of the Raman Spectra of Iron Oxide and Oxyhydroxide Compounds. *J. Raman Spectrosc.* 2011, 42(6), 1335-1339.

(71) Zheng, C. Y.; Zhang, X.; Zhou, Z.; Hu, Z. P. A First-principles Study on the Electrochemical Reaction Activity of 3d Transition Metal Single-Atom Catalysts in Nitrogen-doped Graphene: Trends and Hints. *eScience* 2022, 2, 219-226.

(72) Seh, Z. W.; Kibsgaard, J.; Dickens, C. F.; Chorkendorff, I. B.; Norskov, J. K.; Jaramillo, T. F. Combining Theory and Experiment in Electrocatalysis: Insights into Materials Design. *Science* 2017, 355(6321), eaad4998.

SYNOPSIS TOC